

pubs.acs.org/NanoLett Letter

# Active Tuning of Plasmon Damping via Light Induced Magnetism

Oscar Hsu-Cheng Cheng, Boqin Zhao, Zachary Brawley, Dong Hee Son, and Matthew T. Sheldon



Cite This: Nano Lett. 2022, 22, 5120-5126



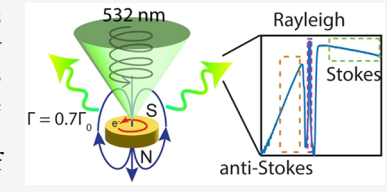
**ACCESS** 

Metrics & More

Article Recommendations

SI Supporting Information

**ABSTRACT:** Circularly polarized optical excitation of plasmonic nanostructures causes coherent circulating motion of their electrons, which in turn gives rise to strong optically induced magnetization, a phenomenon known as the inverse Faraday effect (IFE). In this study we report how the IFE also significantly decreases plasmon damping. By modulating the optical polarization state incident on achiral plasmonic nanostructures from linear to circular, we observe reversible increases of reflectance by up to 8% and simultaneous increases of optical field concentration by 35.7% under 10<sup>9</sup> W/m<sup>2</sup> continuous wave (CW) optical



excitation. These signatures of decreased plasmon damping were also monitored in the presence of an external magnetic field (0.2 T). We rationalize the observed decreases in plasmon damping in terms of the Lorentz forces acting on the circulating electron trajectories. Our results outline strategies for actively modulating intrinsic losses in the metal via optomagnetic effects encoded in the polarization state of incident light.

KEYWORDS: plasmonic, inverse Faraday effect, Raman thermometry, magnetoplasmon

he reversible modulation of plasmonic resonances in metal nanostructures using external stimuli, i.e., "active plasmonics", is currently of great interest for potential applications in sensing, optoelectronic devices, and lightbased information processing.<sup>1</sup> Commonly explored strategies modulate plasmon resonance frequencies by altering the surrounding dielectric environment of nanostructures, for example, with thermoresponsive materials.<sup>2–4</sup> Modification of plasmonic modes based on distance-dependent optical coupling between nanostructures in compliant media under stress and strain has also been demonstrated. 5-7 Alternatively, the optical properties of the metal comprising a nanostructure can be reversibly modulated. Within the Drude model, the complex dielectric function of a metal at angular frequency,  $\omega_t$ is well described in terms of the electrical carrier density, *n*, and the damping constant,  $\Gamma$ , for the carrier oscillations:

$$\varepsilon(\omega) = 1 - \frac{\omega_{\rm p}^2}{\omega^2 + i\omega\Gamma}$$
 (1)

where  $\omega_{\rm p}=\sqrt{\frac{ne^2}{\varepsilon_{\rm o}m_{\rm e}}}$  is the bulk plasma frequency, also depending on the electron charge, e, effective mass,  $m_{\rm e}$ , and vacuum permittivity,  $\varepsilon_{\rm o}$ . Researchers have shown that capacitive surface charging of metals when they are integrated into electrochemical cells results in reversible shifts of their plasmon resonance frequency through the dependence on n. In the time domain, pulsed laser excitation can similarly perturb electronic carrier populations giving rise to transient modulation of plasmonic behavior.  $\frac{12-17}{12}$ 

In comparison, the possibility of actively tuning plasmon damping in the steady state, and the opportunities for manipulating plasmonic behavior, has been studied much less.  $^{18-21}$  In eq 1,  $\Gamma$  reflects several different microscopic

processes connected with the conductivity and mean free path of electrical carriers in the metal such as electron-electron scattering, electron-phonon scattering, surface scattering, and chemical interface damping with surface adsorbates,<sup>23</sup> addition to other loss pathways such as radiation damping  $^{24}$  and Landau damping.  $^{25,26}$  Usually,  $\Gamma$  is considered to be an intrinsic property that is determined by the chemical identity of the metal, 27,28 surface chemistry and morphology, such as the crystal grain size, <sup>29-32</sup> or the modal behavior at a particular frequency, 18,19 e.g., near field localization versus far field outcoupling. However, changes in plasmon damping have a profound impact on the ability of a nanostructure to concentrate optical power in a particular mode, known as the quality factor or "Q" factor. Decreasing  $\Gamma$  lowers the imaginary part of the permittivity, decreasing ohmic losses from carrier motion at the optical frequency and increasing overall optical scattering or reflectance. Lower damping also provides greater field enhancement at subwavelength "hot spots", improving efficiency for localized sensing, photochemistry, or heating via photothermalization.

In a series of recent studies, the Vuong laboratory reported anomalously large magneto-optical (MO) responses from colloidal Au nanoparticles under small magnetic fields (~1 mT) and low intensity circularly polarized (CP) excitation (<1 W/cm<sup>2</sup>).<sup>33,34</sup> The large MO response was attributed to the interaction between external magnetic fields and circulating

Received: February 11, 2022 Revised: June 20, 2022 Published: June 27, 2022





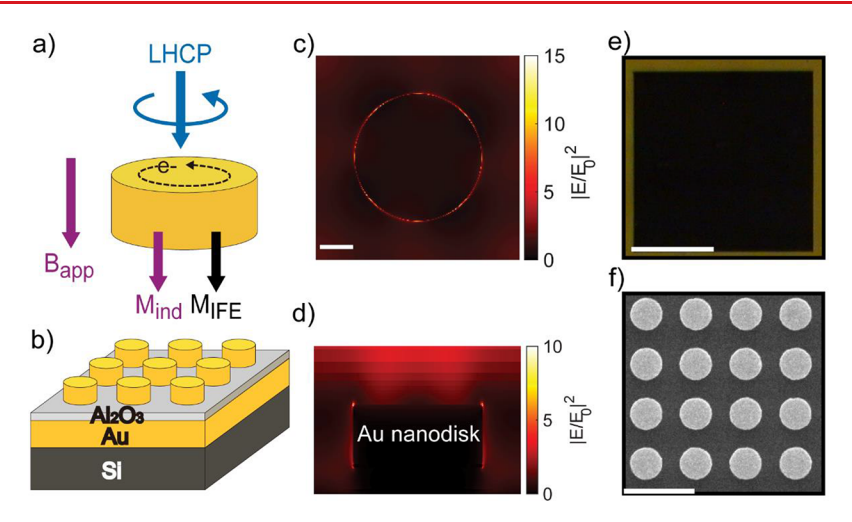


Figure 1. Sample overview. (a) Relationship between incident light helicity, induced electronic motion, induced magnetization from the IFE  $(M_{\rm IFE})$ , and induced magnetization  $(M_{\rm ind})$  from an external static magnetic field  $(B_{\rm app})$  in a plasmonic nanostructure. When incident light has left-handed circular polarization (LHCP),  $M_{\rm IFE}$  and  $M_{\rm ind}$  are parallel. (b) Schematic of the Au nanodisk array sample (not to scale). (c) Top view and (d) side view of the local field enhancement during 532 nm excitation. Width and height are not to scale in (d). (e) Optical image of the array on an Au film (f) SEM image. Scale bars: (c) 100 nm, (e) 40  $\mu$ m, and (f) 1  $\mu$ m.

drift currents in the metal that were resonantly excited during CP excitation (Figure 1a). The authors also reported an apparent increase of the volume averaged electrical conductivity (consistent with decreased damping) when an external magnetic field was aligned with the light-induced magnetic field. Several recent theoretical and experimental magnetic circular dichroism (MCD) studies<sup>35–37</sup> similarly report that the large MCD response in Au colloids is due to circulating electron trajectories during CP excitation that enhance magnetic interactions. Further, Weinmann et al. theoretically describe a decrease in mode damping when rotating surface charge density waves provide magnetization parallel with externally applied magnetic fields, based on the Lorentz forces acting on electrons.<sup>35</sup> The generation of drift currents from coherent charge density waves that circulate in metals during CP optical cycles has been studied extensively theoretically 38-40 and is understood to contribute to optically induced static (DC) magnetism, which is known as the inverse Faraday effect (IFE). 38-44 The phenomenon has been confirmed by our recent experimental study of 100 nm Au nanoparticle colloids which revealed MO activity and optically induced magnetism many orders of magnitude greater than for bulk Au. 45 The circulating currents and consequent magnetization are not present during LP excitation. These studies suggest that CP excitation can act as a source of magnetism for reversible modulation of plasmon damping; however, this mechanism for optical control of damping has not been reported before.

In this study we show that plasmon damping is indeed strongly modified by magnetic interactions, whether magnetism is induced externally using an applied magnetic field or created internally with light via the IFE. We observe that the normal incidence backscattering, i.e., the reflectance, of arrays of nonchiral Au nanostructures is increased by up to 8% (absolute) when controlling the ellipticity of incident light from linearly polarized (LP) to CP during 10<sup>9</sup> W/m² continuous wave (CW) excitation. Further, we query the optical field concentration at hot spots in the metal by taking advantage of recently refined electronic Raman thermometry techniques. 46–53 Localized photothermal heating induces

temperatures  $\sim\!23$  K greater during CP excitation than during LP excitation under an excitation intensity of  $\sim\!10^9$  W/m², suggesting active modulation of optical field enhancement by 35.7% at hot spots. The local heating is further modulated by the presence of an externally applied magnetic field ( $\sim\!0.2$  T), supporting the underlying magnetic origin of these phenomena and allowing estimation of the light-induced effective magnetic fields at hot spots ( $\sim\!1.3$  T). Taken together, our results indicate reversible modulation of the plasmon damping between 10% and 30%, solely by controlling the ellipticity of the incident radiation.

Samples consisting of 100  $\mu$ m  $\times$  100  $\mu$ m arrays of 436 nm diameter by 100 nm height disk-shaped gold nanostructures in a square lattice pattern (700 nm pitch) were deposited on 38 nm thick  $Al_2O_3$  layer on top of 100 nm thick gold films using electron-beam lithography (Figure 1b,e,f; see methods section in Supporting Information). The nanodisk shape supports circulating electronic currents during CP excitation (Figure 1a). Periodic arrays provide high absorptivity across the visible spectrum (Figure 1e, Figure 2a), aiding photothermal heating for the Raman thermometry studies detailed below. The overall sample geometry is achiral and highly symmetric and exhibits no polarization or ellipticity dependence for absorption or scattering (neglecting nonlinear effects), as confirmed by full wave optical simulations (FDTD method, see Supporting Information).

Samples were mounted onto a piezo-driven microscope stage, and confocal maps of the electronic Raman (eR) spectrum (Figure 3a,d) or the backscattering intensity at 532 nm (Figure 3b,e) were collected as a function of position over the edge of an array during linearly polarized (LP) or circularly polarized (CP) excitation. A representative eR spectrum is shown in Figure 2b. In comparison with typical Raman signals that result from inelastic scattering with vibrational modes in a sample, the eR signal is due to inelastic interactions with the electron gas at the metal surface. The broad eR signal therefore provides information about the energetic distribution of electrons, such as their temperature. As clearly seen by comparison of Figure 3a,d and Figure 1c,d, the eR signal is strongest at "hot spots" at the edge of nanodisks where field

Nano Letters pubs.acs.org/NanoLett Letter

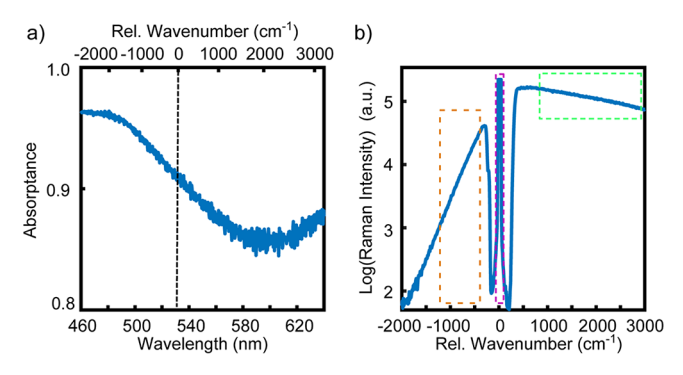


Figure 2. Spectroscopy of gold nanodisk arrays. (a) Absorption spectrum. The dashed line indicates 532 nm. (b) Electronic Raman spectrum during 532 nm CW excitation. Different spectral regions provide information analyzed in this study. Orange box: anti-Stokes signal used for temperature fitting. Purple box: 532 nm backscattering (Rayleigh line, filtered here) used to quantify ellipticity-dependent reflection. Green box: the broad energy distribution of the Stokes region is fit for the plasmon damping,  $\Gamma$ .

enhancement is greatest. In contrast, the sample backscattering, or reflectance (Figure 3b,e), is lower over the array due to pronounced plasmonic absorption, ultimately giving rise to localized photothermal heating.

The backscattering efficiency of the nanodisks is strongly modulated based on the polarization state (ellipticity) of the incident light. As displayed in Figure 3c,f, we compared the backscattered light intensity from different locations over the nanodisk array and the adjacent Au film during LP (dashed trace) or CP (solid trace) excitation. The backscattered signal intensity at either ellipticity was converted to absolute backscattering efficiency by referencing the Au film region to a smooth Ag mirror, in order to rule out any polarization-dependent instrument response (see methods section in Supporting Information for details). In all locations over the array the backscattering efficiency is generally larger for CP versus LP, with a maximum increase of backscattering up to 8% around individual nanodisks during CP excitation.

We rule out the possibility that this trend is due to inherent differences in the ellipticity-dependent scattering efficiency based on sample geometry, because the sample is not chiral. Neglecting optically induced magnetization or other nonlinear effects, the total absorption and scattering of the nanostructure array are expected to show no dependence on beam ellipticity. Indeed, we have performed linear, full wave optical simulations (FDTD method; see Supporting Information) that confirm no difference in the absorption or scattering efficiency based on LP or CP excitation. Further, we measured the backscattered light and intensity as well as the Stokes scattering intensity under LP excitation with the beam polarized along different angles with respect to the nanodisk array (see Figure S3). We observe no significant changes in intensity based on the LP beam orientation angle, indicating these scattering signals do not depend on the beam polarization axis. We hypothesize that the large difference in backscattering efficiency during CP excitation observed experimentally results from ellipticitydependent modulation of the plasmon damping.

Additionally, we have performed simulations of the spatial dependence of the absorption and reflection signal when nonradiative damping,  $\Gamma$ , is decreased (Figure 4). Detailed

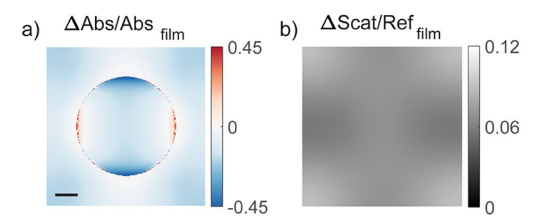


Figure 4. Simulations of the spatial dependence of decreased damping. (a) Relative change in absorption ( $\Delta abs$ ) by decreasing damping from bulk damping,  $\Gamma$ , to  $0.7\Gamma$ , normalized by the absorption ( $Abs_{\rm film}$ ) on a smooth Au film. (b) Relative change in backscattering ( $\Delta Scat$ ) normalized by Au film reflection (Ref\_film) with "Gaussian blurring" assuming a signal resolution with a diameter of  $\sim\!100$  nm. Scale bar in (a): 100 nm.

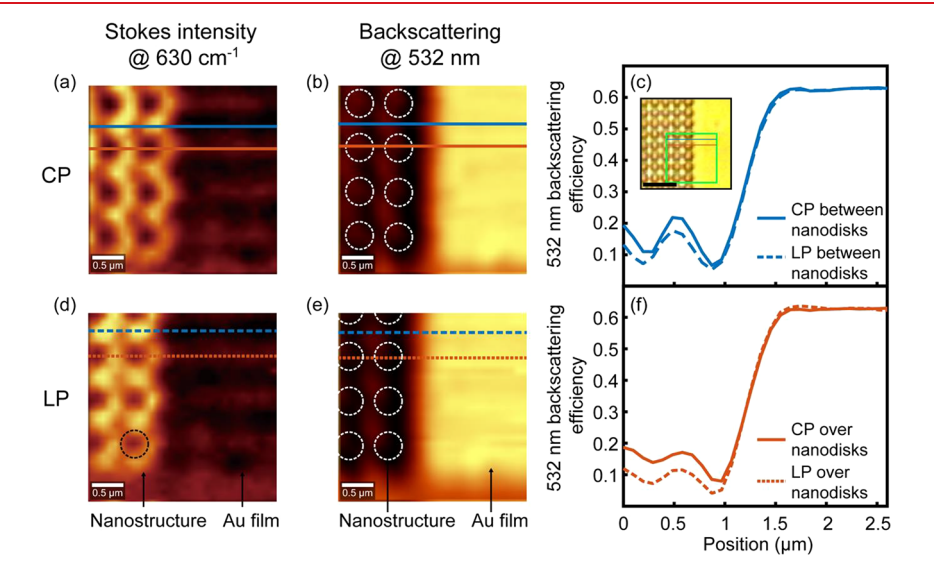


Figure 3. Confocal spectral mapping under different helicities. (a, d) Confocal Raman and (b, e) backscattering intensity map of the gold nanodisk array under 532 nm CW excitation with (a, b) CP or (d, e) LP. (c, f) Line scans of the backscattering efficiency along the region between (blue) or over (red) nanodisks with LP (dashed trace) or CP (solid trace) excitation. Inset: optical image of the sample array. The green box indicates the region of the confocal map. Scale bar:  $4 \mu m$ .

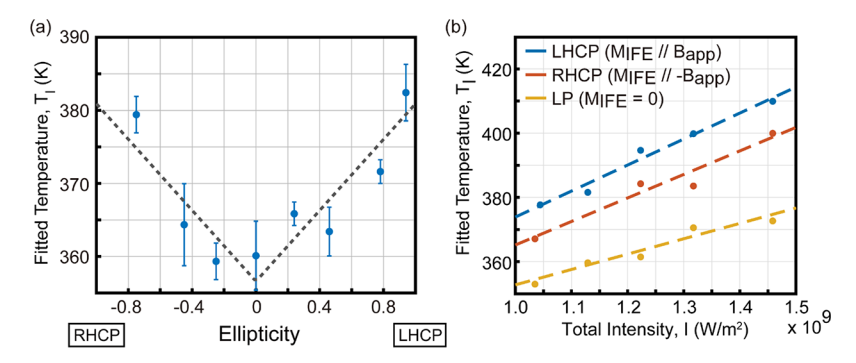


Figure 5. Photothermal heating under the influence of light ellipticity and external magnetic field. (a) Fitted nanostructure temperature as a function of beam 2 ellipticity. The intensity of beam 1 was kept at  $4.8 \times 10^8$  W/m<sup>2</sup>. The intensity of beam 2 was kept at  $9.5 \times 10^8$  W/m<sup>2</sup>. The dashed line is a guide for the eye. See Figure S8 for a detailed explanation of ellipticity and ellipticity angle. (b) Photothermal heating under an external magnetic field and different CP helicities. Fitted nanostructure temperature  $T_0$  as a function of total intensity  $T_0$  with  $T_0$  with  $T_0$  and variable excitation helicity. The magnitude of ellipticity is  $T_0$  for both LHCP and RHCP. The linear fits to each temperature trend are the following: LHCP,  $T_0$  (K) =  $T_0$  (8.1 ×  $T_0$ ) RHCP,  $T_0$  (K) =  $T_0$ ) (8.1 ×  $T_0$ ) 1 + 293; RHCP,  $T_0$  (K) =  $T_0$ ) 1 + 292; LP,  $T_0$  (K) =  $T_0$ ) 1 + 305.

descriptions regarding the simulation can be found in the Supporting Information, section 2. These simulations allow us to quantitatively estimate that a decrease in  $\Gamma$  by  $\sim\!30\%$  in the metal provides an increase in average reflectance (back-scattering) consistent with the data reported in Figure 3c,f of around 6% relative to the film reflectance, as well as the same approximate spatial dependence observed in the confocal maps. The increase in backscattering intensity under CP excitation can be understood intuitively as resulting from an increase in the photonic density of states (PDOS), or equivalently the mode quality (Q-factor), when damping,  $\Gamma$ , decreases. This simulation also clearly emphasizes how the overall average reflectance increases while the absorbed heating power (and hence temperature) at hot spots is also increased with lower damping.

Because decreased plasmon damping results in more concentrated optical fields at hot spots, decreased damping is also expected to lead to more pronounced local photothermal heating. In terms of eq 1, as the damping constant  $\Gamma$  decreases, the imaginary part of the dielectric function  $\text{Im}(\varepsilon(\omega))$  also decreases, giving rise to a larger Q-factor and greater local field enhancement. The local power density for heating, q(x,y,z), depends on field enhancement as  $^{55,56}$ 

$$q(x, y, z) = \frac{\omega}{2} \text{Im}[\varepsilon(x, y, z)] \varepsilon_0 |E(x, y, z)|^2$$
(2)

where E(x,y,z) is the local electric field. Thus, lower plasmon damping provides a net increase of heating power and correspondingly larger temperatures at locations with strong field enhancement. Intuitively, lower damping increases the cross section that funnels light energy into a plasmonic hot spot. See simulations of this effect for the nanodisk array geometry in Figure 4.

Raman signal intensity also depends on local field enhancement, scaling as  $\rm IEI^{4.57}$  Therefore, Raman-based thermometry techniques primarily probe the nanostructure temperature at hot spots. We measured the sample temperature at hot spots by adapting an anti-Stokes (aS) Raman thermometry method developed by Xie et al. Experimentally, it has been shown that the spectral intensity of the aS eR signal,  $S(\Delta\omega)$ , is thermally activated according to a Bose–Einstein distribution. The aS spectrum collected from a sample at an unknown temperature,  $T_b$  can be normalized by a spectrum collected at a known temperature,  $T_0$ , according to

$$\frac{S(\Delta\omega)_{T_l}}{S(\Delta\omega)_{T_0}} = \frac{\exp\left(\frac{-hc\Delta\omega}{k_{\rm B}T_0}\right) - 1}{\exp\left(\frac{-hc\Delta\omega}{k_{\rm B}T_l}\right) - 1}$$
(3)

where h is Plank constant, c is the speed of light,  $\Delta \omega$  is the wavenumber (negative for anti-Stokes), and  $k_{\rm B}$  is the Boltzmann constant. Spectral features that do not change with thermal activation, such as the frequency-dependent signal enhancement factor, cancel out, so that  $T_l$  is the only unknown fitting parameter. We note that the Raman cross section is at least 6 orders of magnitude smaller than the Rayleigh scattering. Therefore, the deposition or removal of energy in the inelastic scattering process has a negligible effect on the electronic energy distribution and does not impact the temperature.

With fixed linear polarization, we measured the aS spectra of samples as a function of excitation power to induce variable amounts of photothermal heating, and we fit for  $T_l$ . The spectra were normalized by a spectrum collected at the lowest possible power that preserved good signal-to-noise ( $I=7.2\times10^6~\mathrm{W/m^2}$ ), with the goal of inducing minimal heating above room temperature, i.e.,  $T_0\approx298~\mathrm{K}$ . We observe that  $T_l$  increases linearly with LP excitation intensity (Figure S5, blue line), in good agreement with many other reports of gold and copper nanostructures. The linear fit to the temperature trend shows a *y*-intercept near room temperature, at the limit of zero incident power, further confirming the accuracy of the thermometry technique. The fitted slope of the trend (4.6 ×  $10^{-8}~\mathrm{K\cdot m^2/W}$ ) describes the "heating efficiency" of the sample under LP excitation.

We determined changes in the sample temperature, and hence modification of the plasmon damping, by measuring the eR response while varying the ellipticity of the excitation beam. However, given the complex spectral dependence of the eR signal, similar procedures as those described for the back-scattering study could not be used to correct for the ellipticity-dependent instrument response. Instead, we devised a dual beam configuration (see methods section in Supporting Information for details). In summary, two separate CW 532 nm laser beams were coincident on the sample. A low power "beam 1" was maintained with linear polarization. A second, higher power "beam 2" was used to induce variable magnetization and damping in the sample by controlling excitation ellipticity. The eR spectrum resultant from beam 1

Nano Letters pubs.acs.org/NanoLett Letter

was isolated and fit for  $T_1$  by collecting a spectrum with both beam 1 and beam 2 incident and then subtracting the spectrum collected with only beam 2 incident. This procedure allowed us to probe the sample temperature using a beam that had nonchanging incident power and linear polarization (beam 1) while the sample was excited with variable ellipticity and power. This procedure also removes possible complications if there is a chiroptic dependence of the scattered Raman signal because there is no scattered light from the CP beam in the fitted spectra. The accuracy of this dual-beam method is confirmed in Figure S5 (red trace). The fitted  $T_1$  is reported as a function of the total incident power of beam 1 and beam 2, with the power of beam 1 held constant and both beams maintained in linear polarization. A similar y-intercept and heating efficiency are observed using either thermometry technique.

We then examined the dependence on the ellipticity of beam 2 while the power of both beams was held constant (Figure 5a). For both right-handed or left-handed circular polarization (RHCP or LHCP),  $T_1$  increases with increasing ellipticity. For the same magnitude ellipticity but opposite helicity, the increase of  $T_l$  is similar. This trend indicates enhanced field concentration at hot spots when the ellipticity-dependent magnetization in the sample is increased. The maximum increase of temperature observed for CP compared with LP is ~23 K. On the basis of the heating efficiency determined under LP excitation (Figure S5, red line), this same temperature increase would be expected if the sample received  $5 \times 10^8 \,\mathrm{W/m^2}$  more incident power. Since the total excitation power was kept constant at  $1.4 \times 10^9$  W/m<sup>2</sup>, we conclude that the switch from LP to CP excitation equivalently increases the heating power at hot spots by 35.7%. We emphasize that field enhancement is not expected to depend on excitation ellipticity, neglecting nonlinear effects, because the sample is not chiral.

We also studied sample behavior under an externally applied magnetic field. For this experiment the ellipticity of beam 2 was kept at either 0 (LP), +0.67 (LHCP), or -0.67 (RHCP). Note that the ellipticity for RHCP was limited to this range based on our experimental geometry (see methods section in Supporting Information). An external magnetic field  $B_{app} = 0.2$ T was applied parallel to the direction of light propagation (Figure 1a), and  $T_1$  was measured as a function of total incident power. As summarized in Figure 5b, the fitted  $T_1$ values are larger under LHCP excitation compared to RHCP, while both polarizations cause greater heating than LP. This effect can be rationalized in terms of the direction between the optically induced magnetization,  $M_{\rm IFE}$ , and the applied magnetic field,  $B_{app}$ . When  $M_{IFE}$  and  $B_{app}$  are antiparallel, as for RHCP, the optically induced circular electron motion is opposite the direction favored by the Lorentz forces from the external magnetic field, resulting in an increase of damping and lower optical field enhancement. In support of this picture, Gu et al. theoretically analyzed the behavior of a free electron gas in a nanoparticle under CP excitation and predicted that the optically induced magnetic moment is enhanced (suppressed) when an external magnetic field is aligned (antialigned), due to the Lorentz forces on individual electrons that perturb their circular movement.<sup>58</sup> As discussed above, theoretical studies also predict decreases in damping when rotating surface charge density waves provide magnetization parallel with externally applied magnetic fields.<sup>55</sup>

The difference in heating efficiency during LHCP and RHCP excitation allows an estimate of the strength of the optically induced magnetization,  $M_{IFE}$ , at hot spots in terms of the magnetization,  $M_{\text{ind}}$ , that results from  $B_{\text{app}}$  (see full calculations in Supporting Information). Assuming that the temperature increase compared to LP excitation is linearly proportional to the net magnetization  $M_{\rm ind}$  +  $M_{\rm IFE}$ , we determine an "effective" magnetic field,  $B_{\rm eff}$ , at hot spots to be 1.3 T for the highest incident power of  $1.45 \times 10^9 \text{ W/m}^2$ and 0.67 ellipticity. Note that Beff is not the magnetic field produced by optically exciting the nanostructure but rather corresponds to the field strength of a hypothetical external magnet that would produce the same magnetization in the nanodisk in the dark as observed during CP optical excitation with no  $B_{\text{app}}$ . This estimate also assumes that  $M_{\text{ind}}$  and  $M_{\text{IFE}}$  are either aligned or antialigned, though their orientation may be more complex microscopically.<sup>42</sup> When normalized for optical power density, the observed magnetization is in good agreement with our previous time-resolved studies of ensembles of Au colloids<sup>45</sup> (Table S1).

Finally, we comment that the plasmon damping can also be estimated directly by fitting to the Stokes side eR spectrum (green box, Figure 2b). As discussed in detail in a recent report from our laboratory,53 the eR spectrum reflects the approximately Lorentzian distribution of nonthermal electron-hole pairs that have been generated during the plasmon damping process, i.e., the natural line width of the excited plasmon. The fitted damping observed under LP  $(1.42 \times 10^9)$  $W/m^2$ ) was 34.1 meV, and the lowest damping observed under CP  $(1.42 \times 10^9 \text{ W/m}^2$ , ellipticity of 0.94) was 31.6 meV. These values can equivalently be reported as a plasmon dephasing time of 19.3 fs (LP) or 20.8 fs (CP) and are comparable to values commonly reported in ultrafast transient absorption studies of Au nanostructures.<sup>21</sup> While this fitted estimate of the ellipticity-dependent change in damping (~8%) is somewhat smaller compared to the estimate based on computational modeling of the sample backscattering study discussed above, both measures consistently indicate a significant decrease of plasmon damping during CP excitation.

In conclusion, we have demonstrated the ability to modulate plasmon damping in achiral plasmonic gold nanodisk arrays by controlling incident light ellipticity. Confocal mapping revealed that CP excitation leads to enhanced efficiency for backscattering, consistent with an overall decrease of damping. A dual-beam Raman thermometry technique quantified localized heating in samples. We observe more efficient photothermal heating when the ellipticity of incident light increases, regardless of helicity (RHCP or LHCP), indicating greater field enhancement at hot spots. The simultaneous increase of scattering and absorption is a telltale signature of decreased damping in plasmonic absorbers. In comparison, under an external magnetic field, RHCP and LHCP excitation provides different amounts of heating. This behavior suggests that the microscopic origin of decreased damping is the interaction between the optically driven coherent electron motion and Lorentz forces from DC magnetic fields, whether magnetic fields are optically induced or externally applied. Our results provide further insight into electron dynamics inside plasmonic nanostructures during CP excitation and suggest multiple new strategies for controllably modulating heating, magnetization, reflectance, damping, and related photophysical effects.

Nano Letters pubs.acs.org/NanoLett Letter

## ASSOCIATED CONTENT

# **5** Supporting Information

The Supporting Information is available free of charge at https://pubs.acs.org/doi/10.1021/acs.nanolett.2c00571.

Experimental methods, full wave electromagnetic simulations, polarization resolved backscattering map, Raman fitting methodology, the accuracy of Raman-fitted temperatures, the accuracy of dual-beam method, determination of optically induced magnetism  $M_{\rm IFE}$  at hot spots, optical setup, and definition of ellipticity (PDF)

# AUTHOR INFORMATION

## **Corresponding Authors**

Dong Hee Son – Department of Chemistry, Texas A&M University, College Station, Texas 77843, United States; Center for Nanomedicine, Institute for Basic Science and Graduate Program of Nano Biomedical Engineering, Advanced Science Institute, Yonsei University, Seoul 03722, Republic of Korea; □ orcid.org/0000-0001-9002-5188; Email: dhson@chem.tamu.edu

Matthew T. Sheldon — Department of Chemistry, Texas A&M University, College Station, Texas 77843, United States; Department of Materials Science and Engineering, Texas A&M University, College Station, Texas 77843, United States; orcid.org/0000-0002-4940-7966; Email: sheldonm@tamu.edu

#### Authors

Oscar Hsu-Cheng Cheng – Department of Chemistry, Texas A&M University, College Station, Texas 77843, United States

**Boqin Zhao** – Department of Chemistry, Texas A&M University, College Station, Texas 77843, United States; orcid.org/0000-0001-9352-9883

Zachary Brawley – Department of Materials Science and Engineering, Texas A&M University, College Station, Texas 77843, United States; orcid.org/0000-0002-0289-7865

Complete contact information is available at: https://pubs.acs.org/10.1021/acs.nanolett.2c00571

# **Author Contributions**

O.H.-C.C. and B.Z. contributed equally. O.H.-C.C. and B.Z. carried out the measurements and analyzed the data. O.H.-C.C. drafted the manuscript. B.Z. and performed the simulations and drafted the Supporting Information. Z.B. fabricated the nanostructures. D.H.S. and M.T.S. supervised the project and participated in the analysis of the data.

## Notes

The authors declare no competing financial interest.

## ACKNOWLEDGMENTS

We thank Prof. Luat Vuong for helpful discussions. This work was funded in part by the National Science Foundation (Grants DMR-2004810 and CHE-2108288). M.T.S. also acknowledges support from the Welch Foundation (Grant A-1886).

# REFERENCES

(1) Jiang, N.; Zhuo, X.; Wang, J. Active Plasmonics: Principles, Structures, and Applications. Chem. Rev. 2018, 118 (6), 3054–3099.

- (2) Gehan, H.; Mangeney, C.; Aubard, J.; Levi, G.; Hohenau, A.; Krenn, J. R.; Lacaze, E.; Felidj, N. Design and Optical Properties of Active Polymer-Coated Plasmonic Nanostructures. *J. Phys. Chem. Lett.* **2011**, *2* (8), 926–31.
- (3) Lei, D. Y.; Appavoo, K.; Sonnefraud, Y.; Haglund, R. F., Jr.; Maier, S. A. Single-particle plasmon resonance spectroscopy of phase transition in vanadium dioxide. *Opt. Lett.* **2010**, *35* (23), 3988–90.
- (4) Kats, M. A.; Blanchard, R.; Genevet, P.; Yang, Z.; Qazilbash, M. M.; Basov, D. N.; Ramanathan, S.; Capasso, F. Thermal tuning of mid-infrared plasmonic antenna arrays using a phase change material. *Opt. Lett.* **2013**, *38* (3), *368*–70.
- (5) Dusemund, B.; Hoffmann, A.; Salzmann, T.; Kreibig, U.; Schmid, G. Cluster Matter the Transition of Optical Elastic-Scattering to Regular Reflection. Z. Phys. D 1991, 20 (1–4), 305–308.
- (6) Su, K. H.; Wei, Q. H.; Zhang, X.; Mock, J. J.; Smith, D. R.; Schultz, S. Interparticle coupling effects on plasmon resonances of nanogold particles. *Nano Lett.* **2003**, *3* (8), 1087–1090.
- (7) Ghosh, S. K.; Pal, T. Interparticle coupling effect on the surface plasmon resonance of gold nanoparticles: from theory to applications. *Chem. Rev.* **2007**, *107* (11), 4797–862.
- (8) Levi, A. F. J. Essential Classical Mechanics for Device Physics; Morgan & Claypool Publishers, 2016.
- (9) Mulvaney, P. Surface Plasmon Spectroscopy of Nanosized Metal Particles. *Langmuir* **1996**, *12* (3), 788–800.
- (10) Sannomiya, T.; Dermutz, H.; Hafner, C.; Voros, J.; Dahlin, A. B. Electrochemistry on a localized surface plasmon resonance sensor. *Langmuir* **2010**, *26* (10), *7619*–*26*.
- (11) Brown, A. M.; Sheldon, M. T.; Atwater, H. A. Electrochemical Tuning of the Dielectric Function of Au Nanoparticles. *ACS Photonics* **2015**, 2 (4), 459–464.
- (12) Wang, X. L.; Guillet, Y.; Selvakannan, P. R.; Remita, H.; Palpant, B. Broadband Spectral Signature of the Ultrafast Transient Optical Response of Gold Nanorods. *J. Phys. Chem. C* **2015**, *119* (13), 7416–7427.
- (13) Zavelani-Rossi, M.; Polli, D.; Kochtcheev, S.; Baudrion, A. L.; Beal, J.; Kumar, V.; Molotokaite, E.; Marangoni, M.; Longhi, S.; Cerullo, G.; Adam, P. M.; Della Valle, G. Transient Optical Response of a Single Gold Nanoantenna: The Role of Plasmon Detuning. *ACS Photonics* **2015**, 2 (4), 521–529.
- (14) Wurtz, G. A.; Pollard, R.; Hendren, W.; Wiederrecht, G. P.; Gosztola, D. J.; Podolskiy, V. A.; Zayats, A. V. Designed ultrafast optical nonlinearity in a plasmonic nanorod metamaterial enhanced by nonlocality. *Nat. Nanotechnol.* **2011**, *6* (2), 107–11.
- (15) Baida, H.; Mongin, D.; Christofilos, D.; Bachelier, G.; Crut, A.; Maioli, P.; Del Fatti, N.; Vallee, F. Ultrafast nonlinear optical response of a single gold nanorod near its surface plasmon resonance. *Phys. Rev. Lett.* **2011**, *107* (5), 057402.
- (16) Sun, C.; Vallee, F.; Acioli, L. H.; Ippen, E. P.; Fujimoto, J. G. Femtosecond-tunable measurement of electron thermalization in gold. *Phys. Rev. B Condens Matter* **1994**, *50* (20), 15337–15348.
- (17) Schirato, A.; Maiuri, M.; Toma, A.; Fugattini, S.; Zaccaria, R. P.; Laporta, P.; Nordlander, P.; Cerullo, G.; Alabastri, A.; Della Valle, G. Transient optical symmetry breaking for ultrafast broadband dichroism in plasmonic metasurfaces. *Nat. Photonics* **2020**, *14* (12), 723–727.
- (18) Yang, J.; Sun, Q.; Ueno, K.; Shi, X.; Oshikiri, T.; Misawa, H.; Gong, Q. Manipulation of the dephasing time by strong coupling between localized and propagating surface plasmon modes. *Nat. Commun.* **2018**, *9* (1), 4858.
- (19) Ueno, K.; Yang, J. H.; Sun, Q.; Aoyo, D.; Yu, H.; Oshikiri, T.; Kubo, A.; Matsuo, Y.; Gong, Q. H.; Misawa, H. Control of plasmon dephasing time using stacked nanogap gold structures for strong near-field enhancement. *Appl. Mater. Today* **2019**, *14*, 159–165.
- (20) Xu, Y.; Qin, Y. L.; Ji, B. Y.; Song, X. W.; Lin, J. Q. Manipulation of Plasmon Dephasing Time in Nanostructure Arrays Via the Far-Field Coupling. *Plasmonics* **2021**, *16* (5), 1745–1754.

- (21) Xu, Y.; Qin, Y.; Ji, B.; Song, X.; Lin, J. Polarization manipulated femtosecond localized surface plasmon dephasing time in an individual bowtie structure. *Opt. Express* **2020**, *28* (7), 9310–9319.
- (22) Besteiro, L. V.; Kong, X. T.; Wang, Z. M.; Hartland, G.; Govorov, A. O. Understanding Hot-Electron Generation and Plasmon Relaxation in Metal Nanocrystals: Quantum and Classical Mechanisms. *ACS Photonics* **2017**, *4* (11), 2759–2781.
- (23) Lee, S. A.; Link, S. Chemical Interface Damping of Surface Plasmon Resonances. *Acc. Chem. Res.* **2021**, *54* (8), 1950–1960.
- (24) Novo, C.; Gomez, D.; Perez-Juste, J.; Zhang, Z.; Petrova, H.; Reismann, M.; Mulvaney, P.; Hartland, G. V. Contributions from radiation damping and surface scattering to the linewidth of the longitudinal plasmon band of gold nanorods: a single particle study. *Phys. Chem. Chem. Phys.* **2006**, 8 (30), 3540–6.
- (25) Li, X. G.; Xiao, D.; Zhang, Z. Y. Landau damping of quantum plasmons in metal nanostructures. *New J. Phys.* **2013**, *15* (2), 023011.
- (26) Kirakosyan, A. S.; Stockman, M. I.; Shahbazyan, T. V. Surface plasmon lifetime in metal nanoshells. *Phys. Rev. B* **2016**, *94* (15), 155429
- (27) Henkel, A.; Jakab, A.; Brunklaus, G.; Sonnichsen, C. Tuning Plasmonic Properties by Alloying Copper into Gold Nanorods. *J. Phys. Chem. C* **2009**, *113* (6), 2200–2204.
- (28) Bobb, D. A.; Zhu, G.; Mayy, M.; Gavrilenko, A. V.; Mead, P.; Gavrilenko, V. I.; Noginov, M. A. Engineering of low-loss metal for nanoplasmonic and metamaterials applications. *Appl. Phys. Lett.* **2009**, 95 (15), 151102.
- (29) Therrien, A. J.; Kale, M. J.; Yuan, L.; Zhang, C.; Halas, N. J.; Christopher, P. Impact of chemical interface damping on surface plasmon dephasing. *Faraday Discuss.* **2019**, 214 (0), 59–72.
- (30) Foerster, B.; Spata, V. A.; Carter, E. A.; Sonnichsen, C.; Link, S. Plasmon damping depends on the chemical nature of the nanoparticle interface. *Sci. Adv.* **2019**, *5* (3), No. eaav0704.
- (31) Bosman, M.; Zhang, L.; Duan, H.; Tan, S. F.; Nijhuis, C. A.; Qiu, C. W.; Yang, J. K. Encapsulated annealing: enhancing the plasmon quality factor in lithographically-defined nanostructures. *Sci. Rep.* **2014**, *4*, 5537.
- (32) Zhang, F. F.; Proust, J.; Gerard, D.; Plain, J.; Martin, J. Reduction of Plasmon Damping in Aluminum Nanoparticles with Rapid Thermal Annealing. *J. Phys. Chem. C* **2017**, *121* (13), 7429–7434.
- (33) Singh, N. D.; Moocarme, M.; Edelstein, B.; Punnoose, N.; Vuong, L. T. Anomalously-large photo-induced magnetic response of metallic nanocolloids in aqueous solution using a solar simulator. *Opt. Express* **2012**, *20* (17), 19214–25.
- (34) Moocarme, M.; Dominguez-Juarez, J. L.; Vuong, L. T. Ultralow-intensity magneto-optical and mechanical effects in metal nanocolloids. *Nano Lett.* **2014**, *14* (3), 1178–83.
- (35) Weick, G.; Weinmann, D. Lifetime of the surface magnetoplasmons in metallic nanoparticles. *Phys. Rev. B* **2011**, 83 (12), 125405.
- (36) Pineider, F.; Campo, G.; Bonanni, V.; de Julian Fernandez, C.; Mattei, G.; Caneschi, A.; Gatteschi, D.; Sangregorio, C. Circular magnetoplasmonic modes in gold nanoparticles. *Nano Lett.* **2013**, *13* (10), 4785–9.
- (37) Kovalenko, O.; Vomir, M.; Donnio, B.; Gallani, J. L.; Rastei, M. V. Chiromagnetoptics of Au and Ag Nanoparticulate Systems. *J. Phys. Chem. C* **2020**, 124 (39), 21722–21729.
- (38) Hertel, R. Theory of the inverse Faraday effect in metals. J. Magn. Magn. Mater. 2006, 303 (1), L1-L4.
- (39) Hertel, R.; Fahnle, M. Macroscopic drift current in the inverse Faraday effect. *Phys. Rev. B* **2015**, *91* (2), 020411.
- (40) Nadarajah, A.; Sheldon, M. T. Optoelectronic phenomena in gold metal nanostructures due to the inverse Faraday effect. *Opt. Express* **2017**, *25* (11), 12753–12764.
- (41) van der Ziel, J. P.; Pershan, P. S.; Malmstrom, L. D. Optically-Induced Magnetization Resulting from the Inverse Faraday Effect. *Phys. Rev. Lett.* **1965**, *15* (5), 190–193.

- (42) Karakhanyan, V.; Lefier, Y.; Eustache, C.; Grosjean, T. Optomagnets in nonmagnetic plasmonic nanostructures. *Opt. Lett.* **2021**, 46 (3), 613–616.
- (43) Sinha-Roy, R.; Hurst, J.; Manfredi, G.; Hervieux, P. A. Driving Orbital Magnetism in Metallic Nanoparticles through Circularly Polarized Light: A Real-Time TDDFT Study. *ACS Photonics* **2020**, 7 (9), 2429–2439.
- (44) Yang, X.; Mou, Y.; Gallas, B.; Maitre, A.; Coolen, L.; Mivelle, M. Tesla-Range Femtosecond Pulses of Stationary Magnetic Field, Optically Generated at the Nanoscale in a Plasmonic Antenna. *ACS Nano* **2022**, *16* (1), 386–393.
- (45) Cheng, O. H. C.; Son, D. H.; Sheldon, M. Light-induced magnetism in plasmonic gold nanoparticles. *Nat. Photonics* **2020**, *14* (6), 365–368.
- (46) Xie, X.; Cahill, D. G. Thermometry of plasmonic nanostructures by anti-Stokes electronic Raman scattering. *Appl. Phys. Lett.* **2016**, *109* (18), 183104.
- (47) Baffou, G. Anti-Stokes Thermometry in Nanoplasmonics. ACS Nano 2021, 15 (4), 5785–5792.
- (48) Hugall, J. T.; Baumberg, J. J. Demonstrating photoluminescence from Au is electronic inelastic light scattering of a plasmonic metal: the origin of SERS backgrounds. *Nano Lett.* **2015**, *15* (4), 2600–4.
- (49) Carattino, A.; Caldarola, M.; Orrit, M. Gold Nanoparticles as Absolute Nanothermometers. *Nano Lett.* **2018**, *18* (2), 874–880.
- (50) Hogan, N.; Wu, S.; Sheldon, M. Photothermalization and Hot Electron Dynamics in the Steady State. *J. Phys. Chem. C* **2020**, *124* (9), 4931–4945.
- (51) Wu, S. X.; Hogan, N.; Sheldon, M. Hot Electron Emission in Plasmonic Thermionic Converters. ACS Energy Lett. 2019, 4 (10), 2508–2513.
- (52) Hogan, N.; Sheldon, M. Comparing steady state photo-thermalization dynamics in copper and gold nanostructures. *J. Chem. Phys.* **2020**, *152* (6), 061101.
- (53) Wu, S. X.; Cheng, O. H. C.; Zhao, B.; Hogan, N. Q.; Lee, A.; Son, D. H.; Sheldon, M. The connection between plasmon decay dynamics and the surface enhanced Raman spectroscopy background: Inelastic scattering from non-thermal and hot carriers. *J. Appl. Phys.* **2021**, *129* (17), 173103.
- (54) West, P. R.; Ishii, S.; Naik, G. V.; Emani, N. K.; Shalaev, V. M.; Boltasseva, A. Searching for better plasmonic materials. *Laser Photonics Rev.* **2010**, *4* (6), 795–808.
- (55) Baffou, G.; Quidant, R. Thermo-plasmonics: using metallic nanostructures as nano-sources of heat. *Laser Photonics Rev.* **2013**, 7 (2), 171–187.
- (56) Govorov, A. O.; Richardson, H. H. Generating heat with metal nanoparticles. *Nano Today* **2007**, *2* (1), 30–38.
- (57) Franzen, S. Intrinsic Limitations on the IEI4 Dependence of the Enhancement Factor for Surface-Enhanced Raman Scattering. *J. Phys. Chem. C* **2009**, *113* (15), 5912–5919.
- (58) Gu, Y.; Kornev, K. G. Plasmon enhanced direct and inverse Faraday effects in non-magnetic nanocomposites. *J. Opt. Soc. Am. B* **2010**, 27 (11), 2165–2173.